Eikonal equation
by a
Discontinuous Galerkin Finite Element Method

A disertation submitted as part of the

Master in Earthquake Engineering and Engineering Seismology

by

Hugo Samuel Sanchez Reyes

Committee:

L. Audin
E. Chaljub
M-P. Doin
D. Jongmans
J. Virieux

June 2014

Année 2013-2014, Master 2 Terre Solide

OSUG

Université Joseph Fourier GRENOBLE

UFR PhITEM

Master Sciences de la Terre et de l'Environnement

Attestation de non plagiat

Je soussigné(e) (Prénom NOM)

Hugo Samuel SÁNCHEZ REYES

Auteur du mémoire (Titre)

Eikonal equation by a Discontinuous Galerkin Finite Element Method

Déclare sur l'honneur que ce mémoire est le fruit d'un travail personnel et que je n'ai ni contrefait, ni falsifié, ni copié tout ou partie de l'œuvre d'autrui afin de la faire passer pour la mienne.

Toutes les sources d'information utilisées et les citations d'auteur ont été mentionnées conformément aux usages en vigueur.

Je suis conscient(e) que le fait de ne pas citer une source ou de ne pas la citer clairement et complètement est constitutif de plagiat, et que le plagiat est considéré comme une faute grave au sein de l'Université, pouvant être sévèrement sanctionnée par la loi.

Fait à Grenoble, France,

Le 13 Juin 2014

Signature de l'étudiant(e)

Eikonal equation by a Discontinuous Galerkin Finite Element Method

Hugo S. Sánchez Reyes

Abstract

Travel time estimation is a very challenging problem in seismology. This seismic attribut is highly important to understand the Earth's interior and the wave propagation. In order to estimate a multi-value travel time field, by tracking the wavefront, the eikonal equation must be solved. However, solving a non-linear Partial Differential Equation, which solution implies a discontinuity propagating (wavefront), is not an easy task. Cheng and Shu (2007), Bokanowski et al. (2011) and Bokanowski et al. (2011) showed that the Discontinuous Galerkin Finite Element Method (DG-FEM) is suitable for wavefront propagation problems. In this work, some assumptions are supplied in order to treat the eikonal equation as a 1D advection, and the DG-FEM is implemented to solve our formulation. Three different numerical examples of wavefront tracking along different media, homogeneous and heterogeneous, are provided to show applications of this methodology. Requirements to extend this work to 2D and 3D are also included.

Résumé

L'estimation des temps de trajet est un véritable défi en sismologie. Cet attribut sismique est essentiel pour comprendre l'intérieur de la Terre et la propagation des ondes. Afin de calculer le champ de temps de trajet, par le suivi d'un front d'onde, il faut résoudre l'équation eikonal. Néanmoins, résoudre une équation différentielle partielle non-linéaire, où la solution implique une discontinuité qui se propage (front d'onde), n'est pas une tâche facile. Cheng and Shu (2007), Bokanowski et al. (2011) et Bokanowski et al. (2014) ont démontré que la Méthode des Elements Finis Galerkin Discontinue (DG-FEM) peut être adaptée avec succès aux problèmes de propagation du front d'onde. Dans ce travail, certaines hypothèses sont fournies afin de traiter l'équation eikonal comme une advection 1D, et la DG-FEM est implémentée pour résoudre notre formulation. Trois exemples numériques différents d'éstimation des temps de trajet, dans des milieux homogènes et hétérogènes, sont fournis pour montrer les applications de cette méthodologie. Les outils nécessaires à l'extension de ce travail en 2D et en 3D sont également fournis en fin de rapport.

Contents

1 Introduction

1.1 Eikonal equation, motivation and context.

Because the Earth is translucid, seismic waves, produced somewhere by a source, propagate through the Earth and can be recorded and detected. Thanks to the study of seismic wave propagation, we can prospect and understand the Earth's interior. The seismograms are records of these several well-distinguished seismic wave packets arriving, at a certain distance from the seismic source, with specific attributs.

One of the most challenging problems in seismology is to predict the source-receiver path which is followed by the waves in presence of wave speed heterogeneities in the medium (Rawlinson et al., 2007) (figure 1). In order to overcome this problem, the time that the waves have been traveling along a certain path is of crucial importance. This key attribut is known as *travel time*, and our work is dedicated to estimate it efficiently and accurately.

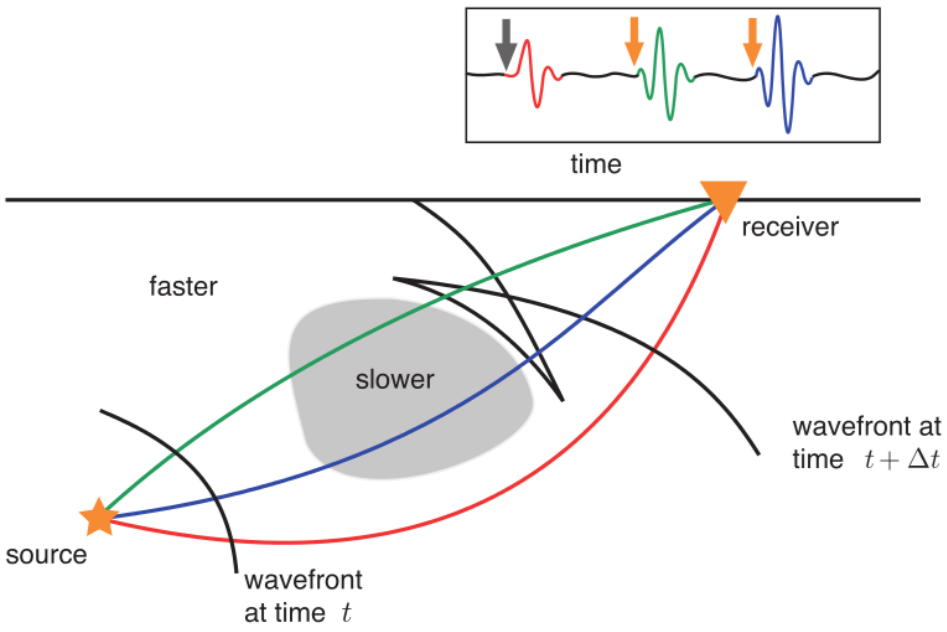

Figure 1: Schematic diagram showing ray paths for a medium containing a slow velocity anomaly. The wavefront triplicates and three arrivals are observed. The ray path for the first, second, and third arrivals are shown in red, green, and blue, respectively. Taken from Hauser et al. (2006).

Techniques to estimate travel times in the Earth have been developed (IASPEI, softwares TTIM and TTLAYER). However, the Earth is heterogeneous, and the presence of continuous or discontinuous lateral changes of the wave speed in the medium may affect, and as a consequence, its corresponding travel time field will also change. Therefore, our motivation is to estimate the travel times beyond this radial approximation. To do so, the *eikonal equation*

$$(\nabla T)^2(\mathbf{x}) = \frac{1}{c^2(\mathbf{x})}, \qquad \mathbf{x} = (x, y, z) \tag{1}$$

which is the non-linear Partial Differential Equation (PDE) describing the link between the gradient of the travel time field $\nabla T(\mathbf{x})$, and the local wave speed $c(\mathbf{x})$ (in a cartesian coordinate system), must be solved.

Due to its importance in many scientific contexts, several efforts to solve the eikonal equation, increasingly more accurate and efficient, have been applied by many authors. In seismology, nice reviews of the strategies used to solve this equations can be found in Rawlinson et al. (2007) and Virieux and Lambare (2014). Recently, in the computational field, Hu and Shu (2004), Cheng and Shu (2007), Bokanowski et al. (2011) and Bokanowski et al. (2014) have shown that a numerical method, known as Discontinuous Galerkin Finite Element Method (DG-FEM), can be effectively implemented to propagate wavefronts. This methodology is related to our PDE's, as the wavefronts can be seen as isochrones of travel times. Furthermore, Hauser et al. (2006) encouragingly showed that applications of this approach, on seismics and seismology, could allow us to estimate accurate first and later arrivals, where the later contain information of great importance for heterogeneous media (figure 1).

This report is organized as follows. Initially, section two introduces where the eikonal equation is derived from. Additionally, a review on the common strategies to solve the PDE's is also provided as a way to set some concepts. Section three is related to the implemented DG-FEM scheme and its characteristics. In section four, some numerical examples of travel time estimation in different 1D media are presented. Results in homogeneous, heterogeneous, and a medium with a low-wave speed zone are shown. Finally, section five discusses our results and describes the potential applications in 2D and 3D.

2 Eikonal equation

To better explain each concept, let us first set as reference an isotropic medium with wave speed heterogeneities, which lengths are relatively larger than the wavelength of the propagating body waves. The coordinate system to use is the cartesian (t, x, y, z). Following Virieux and Lambare (2014), we can consider at a given time T_0 , a set of particles vibrating in phase on a smooth surface, the particles on this surface have the same travel time, $T(\mathbf{x}) = T_0$. If the smooth surface propagates through the medium, the *wavefront* can be seen as isochrones of travel time.

A *ray* between two points (source-receiver), describes the propagation trajectory of the wavefront as the evolution parameter (for instance time) increases. In an isotropic medium, the ray direction is always and everywhere orthogonal to the wavefront surface. Moreover, the wavefront propagates with a local velocity $c(\mathbf{x})$ and, if the medium is isotropic, the gradient of the traveltime field $\nabla T(\mathbf{x})$ is everywhere perpendicular to it, which means parallel to the ray (figure 2).

2.1 From the wave equation to the eikonal equation.

Both, the eikonal and transport equation, are derived from the wave propagation equations. As a first step, we take the general form of the *scalar wave equation*

$$\frac{\partial^2 \mathbf{u}}{\partial t^2} - c(\mathbf{x})\nabla^2 \mathbf{u} = 0. \tag{2}$$

where $\mathbf{u} = u(\mathbf{x}, t)$ is the displacement field, $\mathbf{x} = (x, y, z)$ is the coordinate system, $c(\mathbf{x})$ is the local wave speed vector of the medium, t is the time, and ∇^2 is the Laplacian operator. In this section, boldface symbols are used for vectors and tensor fields. The scalar wave equation is a set of PDE's which can be subjected to the following initial conditions

$$\begin{cases} u(\mathbf{x}, 0) & = u_0(\mathbf{x}), \\ \frac{\partial u(\mathbf{x},0)}{\partial t} & = u_1(\mathbf{x}). \end{cases}$$

On the other hand, the boundary conditions are not easy set due to the different characteristics that these limits can show.

However, equations (2) in heterogeneous media have no analytical solutions and the alternatives are either: 1) to apply a numerical method or 2) to work them out in a specific configuration. As other authors (Chapman, 2004; Cheng and Shu, 2007; Engquist et al., 2002), we will consider a *high-frequency asymptotic solution*, which is built by a source wavelet f, an amplitude factor A^n, and a travel time function $\tau(\mathbf{x})$. Following Qian et al. (2003), when $u_0(\mathbf{x})$ and $u_1(\mathbf{x})$ contain mainly high-frequency [1], the *ansatz*[2] commonly used to approximate the solution to (2) is of the form

[1] *Assumed high-frequency wave:* Wave which wavelength (λ) is substantially shorter than the length of the seismic heterogeneities that characterizes the medium through which they pass.

[2] *Ansatz*: An assumption about the form of an unknown function which is made in order to facilitate the solution.

$$u(\mathbf{x},t) \simeq \sum_{n=0}^{\infty} A^{(n)}(\mathbf{x}) f_n(t-\tau(\mathbf{x})), \qquad f_{n+1}^{'} = f_n, \tag{3}$$

here f is any D'Alambert form function and the wavefront is given by $t = \tau(\mathbf{x})$. Now, let us suppose as solution the zero-order approximation of (3) in terms of the Fourier domain, specifying the Fourier transform of $f(t)$ as $f(\omega) = \int_{-\infty}^{\infty} f(t) e^{i\omega t} dt$. The corresponding solution is

$$u(\mathbf{x},\omega) = S(\omega) e^{i\omega T(\mathbf{x})} A_0(\mathbf{x}), \tag{4}$$

where $\omega = 2\pi/t$ is the angular frequency, $S(\omega)$ is the source wavelet, $T(\mathbf{x})$ are the travel time functions and $A_0(\mathbf{x})$ the amplitude coefficients. We distinguish here that neither traveltimes nor amplitudes depend on frequency.

Taking $u(\mathbf{x},\omega)$ from (4) as solution, it is possible to develop separately the Laplacian and the second-order time derivative in (2).

From the vectorial calculus we know that

$$\nabla^2 \mathbf{u} = \nabla(\nabla \cdot \mathbf{u}) = (\nabla \cdot \nabla)\mathbf{u} + (\mathbf{u} \cdot \nabla)\nabla + \nabla \times (\nabla \times \mathbf{u}) + \mathbf{u} \times (\nabla \times \nabla), \tag{5}$$

and developing

$$\begin{aligned} \nabla^2 \mathbf{u} =& \nabla^2 A_0(\mathbf{x}) e^{-i\omega(T(\mathbf{x}))} - i\omega \nabla T(\mathbf{x}) \cdot \nabla A_0(\mathbf{x}) e^{-i\omega(T(\mathbf{x}))} - i\omega \nabla A_0(\mathbf{x}) \cdot \nabla T(\mathbf{x}) e^{-i\omega(T(\mathbf{x}))} \\ & - i\omega A_0(\mathbf{x}) \nabla^2 T(\mathbf{x}) e^{-i\omega(T(\mathbf{x}))} - i\omega^2 A_0(\mathbf{x}) \nabla T(\mathbf{x}) \cdot \nabla T(\mathbf{x}) e^{-i\omega(T(\mathbf{x}))}, \end{aligned} \tag{6}$$

on the other hand,

$$\frac{\partial^2 \mathbf{u}}{\partial t^2} = -\omega^2 A(\mathbf{x}) e^{-i\omega(T(\mathbf{x})+t)}. \tag{7}$$

As our assumption is a high-frequency solution, the terms in ω^0 are neglected. Inserting (6) and (7) into the wave equation (2), and dividing through the common term $e^{-i\omega(T(\mathbf{x}))}$, the wave equation can be reduced to

$$\omega^2 A_0(\mathbf{x}) \left[(\nabla T)^2(\mathbf{x}) - \frac{1}{c^2(\mathbf{x})} \right] + i\omega [2\nabla A_0(\mathbf{x}) \cdot \nabla T(\mathbf{x}) + A_0(\mathbf{x}) \nabla^2 T(\mathbf{x})] + \nabla^2 A_0(\mathbf{x}) = 0. \tag{8}$$

Taking the real term from (8), and dividing it through $A_0(\mathbf{x})\omega^2$, we obtain

$$\frac{\nabla^2 A_0(\mathbf{x})}{A_0(\mathbf{x})\omega^2} + (\nabla T)^2(\mathbf{x}) - \frac{1}{c^2(\mathbf{x})} = 0, \tag{9}$$

and recalling once again that this approach considers high-frequency wave propagation ($\omega \to \infty$), the terms in ω^2 are set to zero and the eikonal equation is derived

$$\boxed{(\nabla T)^2(\mathbf{x}) = \frac{1}{c^2(\mathbf{x})}.} \tag{10}$$

It should be highlighted that the neglected term depending on ω may affect further approximations where the frequency is finite. The eikonal equation (10) states that the gradient of the traveltime field ($T(\mathbf{x})$) at any time and position is equal to the local *slowness*, understanding the slowness as $s(\mathbf{x}) = 1/c(\mathbf{x})$. Additionally, $T(\mathbf{x})$ is a time function which describes the evolving wavefronts (figure 2) when T is constant.

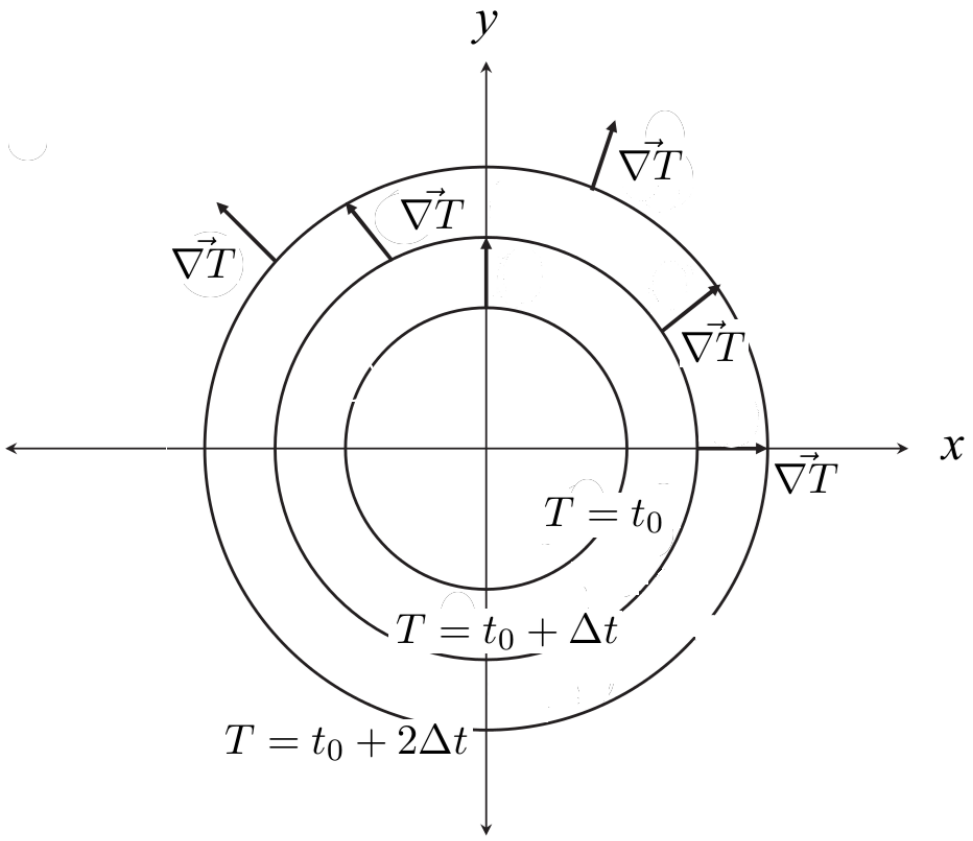

Figure 2: Wavefront propagating along the (x, y) plane. The smooth surface (circles) represent the evolution of the wavefront after several time steps. The gradient ∇T, always orthogonal to the wavefront, points the direction of propagation. Modified from Osher and Fedkiw (2003).

The eikonal equation (10) is a set of non-linear PDE's which belong to the Hamilton-Jacobi (H-J) variety (see section 2.4 of this work) (Virieux and Lambare, 2014). Unfortunately, in heterogeneous media these equations have no analytical solutions.

There are two different points of view to describe the physics of the eikonal equation. The first is the Lagrangian formulation, which is focused on describing the wavefront propagation by tracking the behavior of a particle along a trajectory (or ray). Techniques that solve the eikonal equation by a Lagrangian formulation are known as ray based methods. On the contrary, the Eulerian formulation describes the traveltime field evolution along the whole medium as the wavefront propagates. Grid based techniques are the ones derived from the Eulerian formula-

tion. We now provide a review of each formulation, as well as pros and cons of some currently used techniques.

2.2 Ray tracing, a Lagrangian formulation.

Traditionally, ray tracing has been a way to work out the eikonal equation by using the method of *characteristics*. Its popularity relies on the simplistic estimation of other wave-related parameters as a consequence of the resulting estimated ray. This technique is based on 3D trajectories called *characteristics* $\mathbf{x} = \mathbf{x}(\tau)$, where τ is the evolving parameter along the one a new set of non-linear Ordinary Partial Equations (ODEs) must be verified.

The ODEs come from the reformulation of equation (10). We set H_n as the Hamiltonian of the system, which form is either $H_1(\mathbf{x}, \mathbf{p}) = \mathbf{p}/(2\mathbf{s}^2) = 1/2$ (Chapman, 2004), or $H_2(\mathbf{x}, \mathbf{p}) = 1/2(\mathbf{p}^2 - \mathbf{s}^2) = 0$ (Virieux and Farra, 1991). In this formulation, $\mathbf{x}$ is the position of the particle, $\mathbf{p} = \nabla T(\mathbf{x})$ is the gradient of the traveltime and, $s(\mathbf{x}) = \mathbf{s} = 1/(c(\mathbf{x}))$ is the slowness vector. As for the case of particle's motion (Thorton and Marion, 1994), the Lagrangian formulation of the H-J system of equations can be written as

$$\begin{aligned} \frac{d\mathbf{x}}{d\tau} &= \frac{\partial H}{\partial \mathbf{p}} \\ -\frac{d\mathbf{p}}{d\tau} &= \frac{\partial H}{\partial \mathbf{x}} \\ \frac{dT}{d\tau} &= \mathbf{p}\frac{\partial H}{\partial \mathbf{p}}, \end{aligned} \tag{11}$$

These seven equations (11), where $\tau = dT/(\mathbf{p}\partial H/\partial \mathbf{p})$ depends on the form of the chosen Hamiltonian, define a 6D space known as *phase space*. The values for constant Hamiltonian conform an hypersurface[3] in the phase space. This surface can be considered as a level set of general functions $H(\mathbf{x}, \mathbf{p})$ (Osher et al., 2002). Then, rays are solutions to the system, which are represented as bicharacteristic strips (figure 4) contained in the hypersurface.

There are two principal categories among ray tracing schemes: by 1) shooting and by 2) bending (figure 3). The shooting method is an iterative initial value problem, where the two point path is the unknown. Several starting direction are initialized at the source point and the corresponding rays are tracked by verifying the ray tracing equations at each step of the evolving parameter. On the other hand, the bending method performs iteratively adjustments to the initial arbitrary ray between source and receiver until the solution is a true path.

Advantages of ray tracing methods are their high accuracy and efficiency in homogeneous media, even in the presence of interfaces. Even the difficulty of having a 6D system has been tackled by strategies which choose as evolution parameter one spatial variable, Cerveny, 2001 introduced the idea of paraxial rays. Parameters as attenuation, amplitude and geometrical spreading are easy to compute once the true path is known (Hauser et al., 2006). Nevertheless, even when the estimation of a certain ray is a fast process, the main disadvantage is to find the

[3] *Hypersurface*: In algebraic geometry, an hypersurface in projective space of dimension n, is an algebraic set of purely dimension $n-1$. This hypersurface in the phase space is also called the *Lagrangian manifold.*

correct initial direction of the ray which would lead to a specific receiver (figure 3). Estimating the correct initial direction becomes an optimization problem. In addition, the obtained ray between source and receiver does not guarantee to be a first or later arrival, which is a limited unpredictable sampling of the medium.

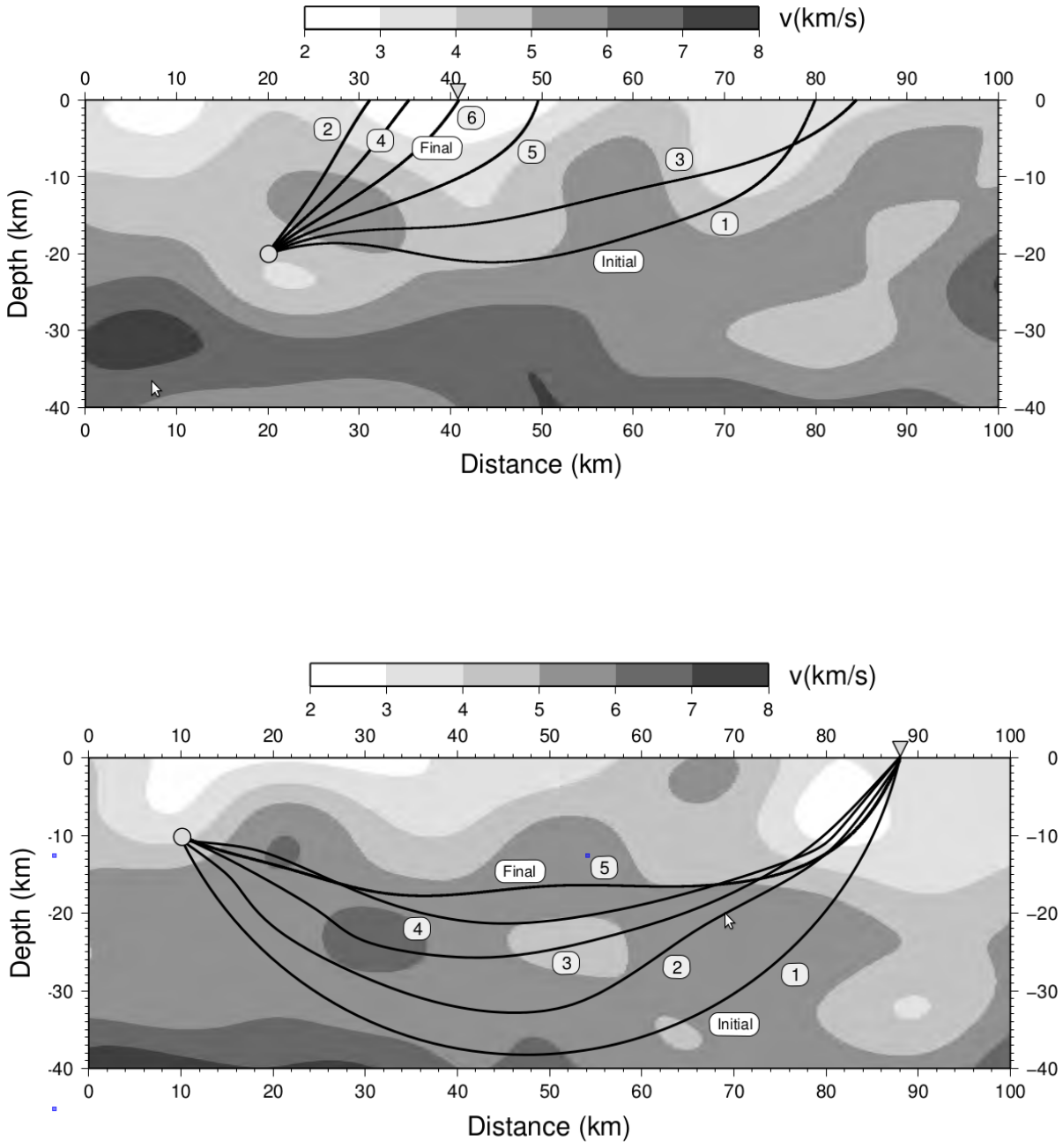

Figure 3: Ray tracing methods. On the upper figure we ilustrate the shooting method. On the second plot, the bending method is shown. Taken from Rawlinson et al. (2007).

2.3 Wavefront tracking, a Semi-Lagrangian formulation.

An alternative technique is focused on tracking the wavefront by iteratively local ray tracing. First, a set of points, located in the normal space, describing the initial wavefront is represented in the phase space by a bicharacteristic strip. At each time step, the iterative process evolves by verifying the local ray tracing equations and the updated locations are again translated into the phase space.

As the wavefront evolves the distance between rays increses or dicreases and an adaptitive ray density criteria is needed (figure 4). If the ray density is too high, the number of rays is decimated. On the contrary, if the ray density is too low, points along the phase space (rays in normal space) are added by interpolation (considering a metric distance criterion) (Vinje et al., 1993; Hauser et al., 2006; Virieux and Lambare, 2014).

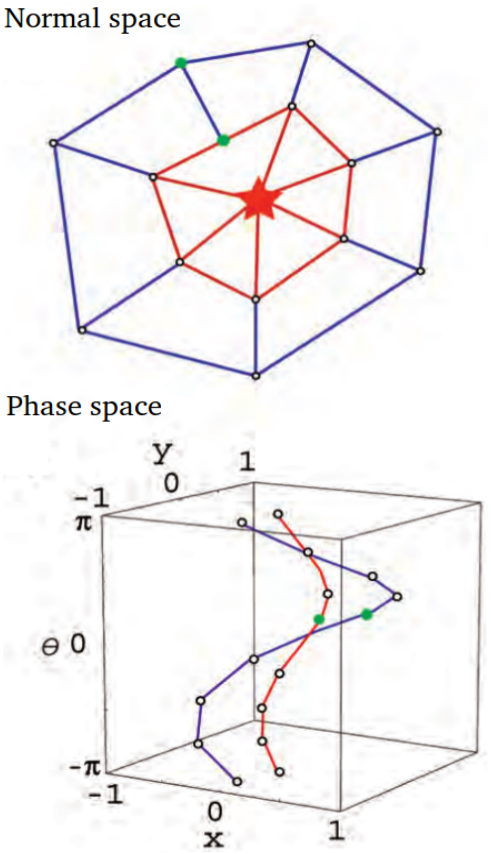

Figure 4: Top) wavefronts in normal space and down) their bicharacteristic strip in phase space. A point (green) is inserted if the phase space distance between two neighbouring points is above a certain threshold. Modified from Hauser et al. (2006).

Local ray tracing is efficient at tracking the wavefront and it clearly overcomes the disadvantages of shooting and bending rays. However, the true problem to achieve is to mantain an adequate ray density, which means, spatial sampling of the wavefronts.

2.4 Travel time estimation, an Eulerian formulation.

Travel time estimation in at fixed points was first promoted by Vidale (1988, 1990). The goal of using an Eulerian formulation is to estimate the travel time at every point of a grid which spans the medium, instead of sampling the medium by rays. We must recall first that the eikonal equation belongs to a H-J variety. Let us now state the static non-linear Hamilton-Jacobi PDE as follows (Virieux and Lambare, 2014)

$$H(\mathbf{x}, \nabla_{\mathbf{x}} T(\mathbf{x}, t)) = 0, \tag{12}$$

and contrary to the Lagrangian formulation, the traveltime field is estimated at every point of a grid that discretizes the medium, while its gradient does not necessarily exist at this points. The traveltime field estimated by a grid based methods implicitly contains the wavefront location (i.e.

isochrons) and all possible rays can be found by tracking the $\nabla_{\mathbf{x}} T(\mathbf{x})$ going from the receiver to the source (figure 2) (Rawlinson et al., 2007).

Grid based schemes have important advantages. As these schemes investigate all possible trajectories, the difficulty that ray tracing methods have to find the true ray path is solved. The level of accuracy and efficiency of these methods to tackle practical problems is enough. By estimating the traveltime at every fixed location along the grid, diffractions in ray shadow zones is well achieved. Finally, in media with continuous heterogeneities the approximated solution always corresponds to first arrivals.

However, all the advantages come with a tradeoff. The accuracy in grid based methods is dependent on grid spacing size. As a consequence, computing costs will dramatically increase when accurate traveltimes are needed, specially for 3D applications. Two of the currently used practical schemes are now introduced.

Fast Sweeping and Fast Marching Methods.

The Fast Sweeping Method (FSM) is an iterative method wich uses an upwind finite difference stencil and applies Gauss-Seidel[4] iterations with alternating sweeping ordering to solve the discretized system (Zhao, 2005).

Each sweeping ordering follows a family of characteristics of the eikonal equation in a certain direction. Then, needed sweeping directions are at least four in a 2D medium, while in 3D the minimum is six. The iterations are not dependent on the grid size and its implementation to 2D and 3D is relatively straightforward.

However, as shown in figure 6, the solution of the static H-J equation is a single-value first-arrival. Moreover, errors may be induced by singularities at boundaries (Quian et al., 2003).

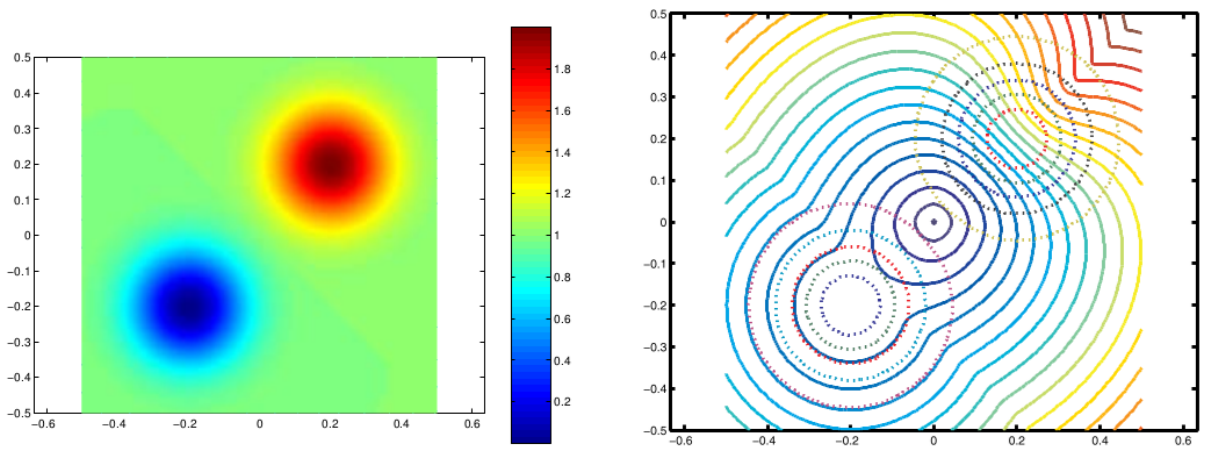

Figure 5: Applied FSM in a 2D medium. On the left, the velocity model proposed for the propagation of the wavefront. On the right, resulting wavefront propagation (solid line) and velocity field (dashed line). Modified from Zhao (2005).

[4] *Gauss-Seidel method*: Known also as method of successive displacement, is an iterative method used to solve a linear system of equations. It is similar to the Jacobi method. Convergent solutions are only guaranteed if the matrix is either diagonally dominant, or symmetric and positive definite.

Another Eulerian approach technique is the Fast Marching Method (FMM). Sethian (1999) introduced the idea of using the level set concepts to transform the wavefront tracking into an stationary boundary problem (figure 6).

In this method, an initial wavefront is defined in the normal space, it is also represented as a surface contained in an hypersurface in the phase space. Then, the goal is to detect the surface and its evolution in the phase space as it elvolves. The evolved surface in the phase space allows us to know the location of the wavefront in the normal space.

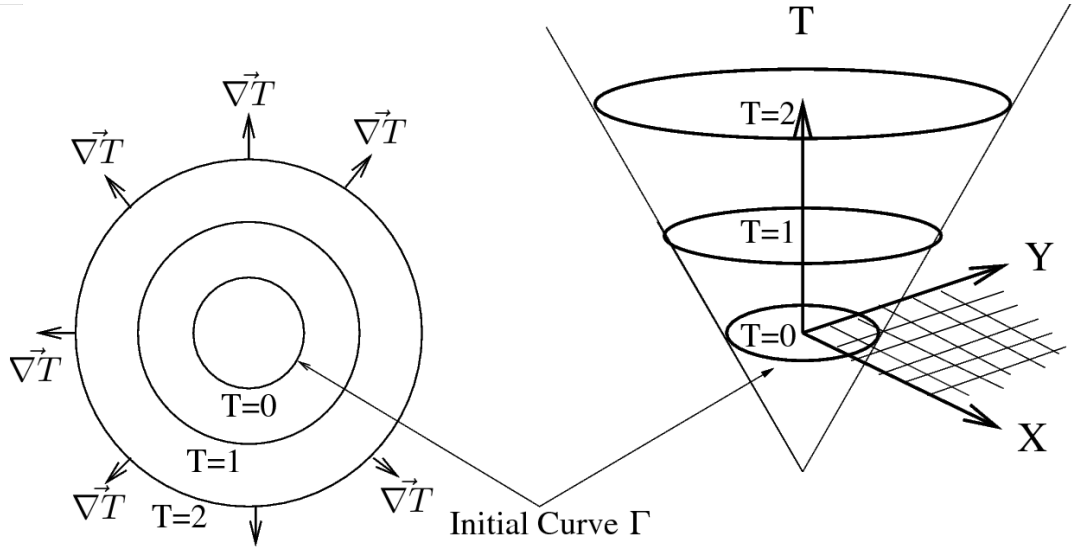

Figure 6: Fast Marching Method. The position of the wavefront in the normal space is set into an initial value problem of the corresponding zero level set. Taken from Sethian (1999).

The traveltime $T(\mathbf{x})$ in the FMM becomes a stationary boundary problem (Sethian, 1999), where the grid is dicretized and the level set equations (13) have to be solved by an efficient numerical method. This method relies on the equations

$$\begin{aligned} \phi_t + N\nabla\phi &= 0, \\ \phi(\mathbf{x}, t=0) &= \phi_0(\mathbf{x}), \end{aligned} \tag{13}$$

where, ϕ is a higher dimension function describing how the initial position of the wavefront (zero level set) propagates, x the position, t the time, and N is the term that describes the speed of propagation in the outward orthogonal direction. Equations (13) are the level set equations, that expands $\phi(\mathbf{x}, t)$ (traveltime field) along the orthogonal trajectory to the interface direction. In this method, the causality of the solution has to be always in mind and upwind finite differences are the most suitable scheme (Osher et al., 2002).

Both methods have shown impressive applications in seismology, wich suggest that the Eulerian formulation allow us to obtain first-arrival traveltime. Thanks to the monotonic evolution of the traveltimes (always increasing from the source), ray trajectories can be traced back from the receiver down to the source. Nevertheless, as mentioned by Virieux and Lambare (2014), when a receiver location does not match a grid node, the corresponding trajectories of first-arrival traveltimes could not be true rays, especially in media with sharp discontinuities. Finally,

we point out again that FSM and FMM approximate only first-arrival solutions and in some cases one may be interested in multiple arrivals.

We have already seen that the Eulerian formulation is the preferred way to work out the PDE's. However, the single-valued solution obtained from the non-linear static H-J equation is not what we are seeking in complex media. Let us then define a solution capable of multi-valued travel-times.

Multi-valued Travel-times.

Considering solutions with multi-values is a step further on complexity. The strategy to solve this problem must rely on the Eulerian formulation, which is more stable due to the fixed sampling of the wavefront. We realize that the wavefront must be correctly tracked. Nevertheless, solution to the static H-J (12) presents problems when the swallowtail effect, or folded wavefront, is caused by the presence of multiple travel-times.

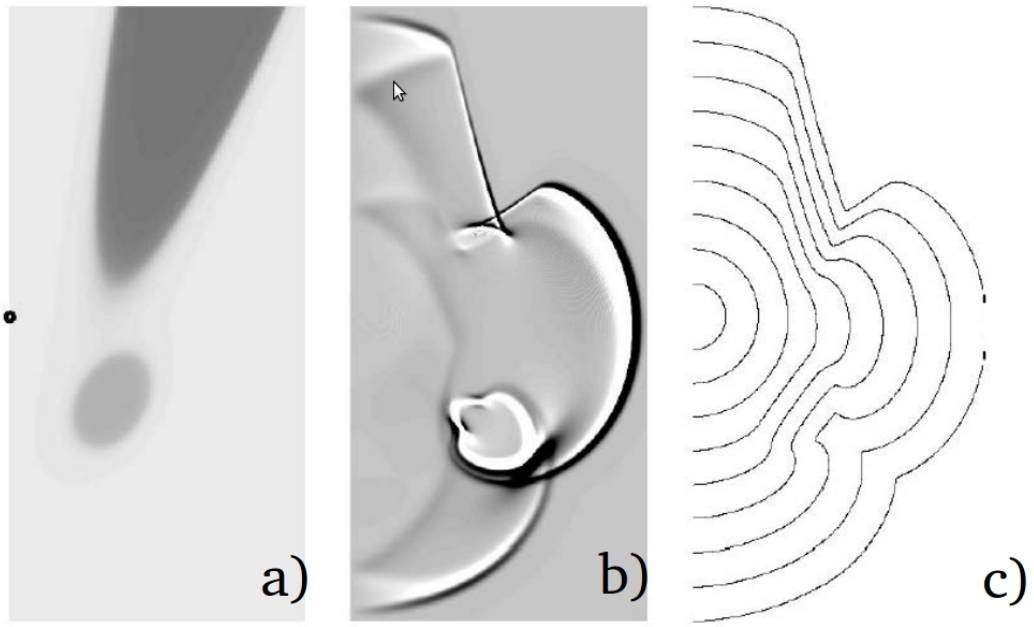

Figure 7: Example on the importance of multi-value travel-times estimation. a) Shows a proposed velocity model with two zones of low velocity (gray), and a point source (black dot). b) Corresponds to the correct solution with multi-value travel-times, the wavefront is folded due to the low-velocity zones. c) Plots the single-value first-arrivals obtained by solving the static non-linear H-J equation by a grid based method.

As shown in figure 7, it is clear that the called *viscous* [5] solution of (12) corresponds to the enveloping first-arrivals, and that important information related to heterogeneties is lost. If the idea of representing the wavefront in a projective phase space is applied, thanks to the Liouville Theorem we will be able to distinguish multiple arrivals in the phase space (bicharacteristic unfolded strip). In the phase space, the wavefront is always a single-valued (figure 8).

[5] *Viscous solution*: Crandall and Lions (1983, 1984) showed that a "viscous" solution to a PDE is the one that follows a minimal entropic criterion. In the eikonal equation, this solution exists and it is unique (Virieux and Lambare, 2014).

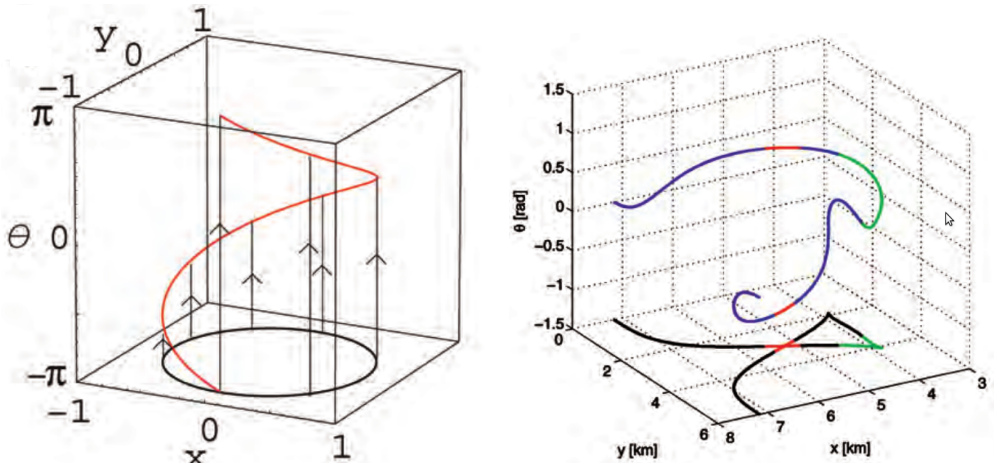

Figure 8: Different Wavefronts in normal and phase space. On the left, a circular wavefront (black line) and its corresponding bicharacteristic strip (red line) in phase space. On the right, swallowtail effect on a wavefront. The intersecting segments in normal space (red lines) do not intersect each other in phase space. The sharp corners in normal space (green segments) are given by a smooth representation in phase space. Modified from Hauser et al. (2006).

However, in order to use this representation in the phase space, the eikonal equation has to be treated as a dynamic H-J PDE instead of a static H-J. Several ways can be followed to go from the static to the dynamic PDE, we mention the simplest. Consider a new function $\phi(x, y, z, t) = T(x, y, z) - t$, which is nothing but the substraction of the running time t, from the traveltime $T(x, y, z)$. Then, the traveltime field can be expressed as

$$T(x, y, z) = \phi(x, y, z, t) + t, \tag{14}$$

and inserting (14) into (10) we derived the dynamic H-J PDE,

$$\boxed{\frac{\partial \phi(\mathbf{x}, t)}{\partial t} \pm c(\mathbf{x}) |\nabla_{\mathbf{x}} \phi(\mathbf{x}, t)| = 0, \qquad \mathbf{x} = (x, y, z).} \tag{15}$$

The structure of this last equation (15) can be linked to the *advection*[6] equation under some assumptions. In section 3.2, we explain in more detail how equation (15) can be treated as the 1D advection equation.

As for the Lagrangian formulation, there are also many strategies to solve these PDE's. It is important to mention the level set method applied by Sethian (1999). This method was built in the computational field, where the motivation was to track evolving functions and their level sets. The concepts involved in this method fit exactly with the idea of a propagating wavefront.

The representation in the phase space requires an additional component in order to unfold the wavefront. Using this form of Hamiltonian, the phase ($\phi(t, \mathbf{x}, \mathbf{p})$) fulfills the Liouville equation. The resulting four dimensional zero level set functions will describe intersections in the 6D phase space. When the intersections are back-projected to the standard space we can locate the corresponding wavefront, even in presence of swallowtail effects.

[6] *Advection*: Is a transport mechanism of a substance.

It is certainly difficult to deal with a 4D level set functions in a 6D phase space, and it represents a numerical challenge. Even reducing the variables from 6 to 5 by just taking into account the modulus of the slowness vector ($\phi(t, \mathbf{x}, ||\mathbf{p}||)$) the result remains expensive. Strategies as the paraxial approach have been also applied for this method (Quian et al., 2003), where a consideration of only vertical propagation ends up with a 2D level set system of equations for a 2D medium (x, y) (Virieux and Lambare, 2014).

In this work we decide to follow the approach shown by Cheng and Shu (2007), Bokanowski et al. (2011),Bokanowski et al. (2014), where insted of trying to solve the reduced level set equation system, the dynamic H-J PDE's is solved by a Discontinuous Galerkin Finite Element Method. Using this numerical scheme Cheng and Shu (2007) has prooved that a multi-valued travel-times solution can be obtained, and that the solution can even deal with discontinuities in the velocity field.

We shall consider a simple 1D geometry in the development of the DG-FEM scheme in order to understand how the propagation of a discontinuity (jump) could be performed along a discrete grid. We, therefore, shall describe the DG-FEM for a 1D discrete medium.

3 Numerical solver: DG-FEM

When an analytical solution of a PDE can not be found, a numerical method has to be implemented to approximate the solution, $\mathbf{u}(\mathbf{x}, t)$. The approximated solution, $\mathbf{u}_h(\mathbf{x}, t)$ is defined as the estimated solution obtained by applying a certain numerical method. There are several numerical methods that can be used to discretize PDE's. In order to choose the most suitable method for a PDE, we require to know how the approximated solution will be obtained and, in which sense the PDE is being satisfied by the estimated solution. Additionally, computational costs, efficiency and stability problems should be also taken into account to make the best profit of the chosen method (Hesthaven and Warburton, 2008).

Among the methods that are usually used to solve the PDE's we could mention as examples: Finite Difference Method (FDM), Finite Volume Method (FVM), Finite Element Method (FEM) and, the one we are interested in, Discontinuous Galerkin Finite Element Method (DG-FEM). Each method has different ways to discretize the differential operators and the physical domain and to approximate the solutions. These specific schemes have advantages and disadvantages dealing with certain problems. In table 1, we enlist some of the generic characteristics of each method that help to support our choice of the DG-FEM as the suitable numerical scheme to work with the eikonal equation.

In a PDE as the eikonal equation (15), the unknown function is dependent on several variables. Considering an unknown scalar function $\mathbf{u} = u(\mathbf{x}, t)$, the values of $\mathbf{u}$ depend on the independent variables $\mathbf{x}$, the position, and t, the time.

The physical domain Ω, can be discretized by a grid of elements. The discretized physical domain Ω_h is then given by

$$\Omega \simeq \Omega_h = \bigcup_{k=1}^{K} D^k, \tag{16}$$

where K is the total number of elements. Then, we will desire to know the respective local solution $u_h^k(\mathbf{x}, t)$ for each element D^k. The order of the local solution depends on the order of the local polynomial interpolation used to approximate the solution. The convergence rate improves by incrementing the order of interpolation polynomials, p, or by decreasing the size of the element h.

Hu and Shu (2004), Cheng and Shu (2007) and Bokanowski et al. (2011, 2014) have shown that the most suitable method to address wavefronts is the one that can ensure simultaneously a flexible element size, and considers the underlying dynamics of the PDE. This specific method is called the Discontinuous Galerkin Finite Element Method (DG-FEM). We now follow Hesthaven and Warburton (2008) and Cheng and Shu (2007) to build our scheme and notation.

Table 1: Generic properties of: Finite Difference Methods (FDM), Finite Volume Methods (FVM), Finite Element Methods (FEM), and Discontinuous Galerkin Finite Element method (DG-FEM).$\surd$ is success and $\times$ is deficiency in the method. A ($\surd$) reflects that the method, with modifications, is capable of solving such problems but remains a less natural choice (Hesthaven and Warburton, 2008).

Method	Complex geometry	High order accuracy and $h-p$ adaptivity	Explicit semi-discrete form	Conservation laws	Eliptic problems
FDM	$\times$	$\surd$	$\surd$	$\surd$	$\surd$
FVM	$\surd$	$\times$	$\surd$	$\surd$	($\surd$)
FEM	$\surd$	$\surd$	$\times$	($\surd$)	$\surd$
DG-FEM	$\surd$	$\surd$	$\surd$	$\surd$	($\surd$)

3.1 The Discontinuous Galerkin Finite Element Method.

In the DG-FEM the element's position should be located as $D^k = [x^k, x^{k+1}]$, and in order to ensure a local approximation $u_h^k(\mathbf{x}, t)$, the unknown variables $\mathbf{u}$ at the nodes $\mathbf{x}^k$, are duplicated (see figure 9) as follows (Hesthaven and Warburton, 2008)

$$\mathbf{u}_h^k = [u^1, u^2, u^2, u^3, \ldots, u^{K-1}, u^K, u^K, u^{K+1}]^T. \tag{17}$$

Therefore, if we work in 1D, the local solution can be approximated as

$$x \in D^k: \qquad u_h^k(x) = u^k \frac{x - x^{k+1}}{x^k - x^{k+1}} + u^{k+1} \frac{x - x^k}{x^{k+1} - x^k} = \sum_{i=0}^{1} u^{k+i} \ell_i^k(x) \quad \in V_h. \tag{18}$$

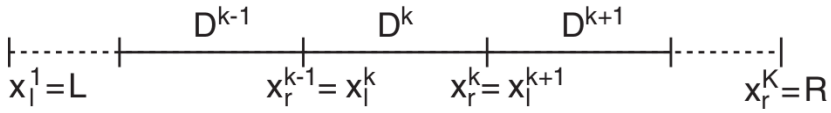

Figure 9: Schematic physical domain discretized by a Finite Elements. The local solution u_h^k is duplicated in the interface between elements. The dotted line represents the first and last element, L and R correspond to the boundary coordinates. Taken from Hesthaven and Warburton (2008).

where the space of basis functions is defined as $V_h = \bigoplus_{k=1}^{K} \{\ell_i^k\}_{i=0}^{1}$, with the linear interpolation functions

$$\ell_i^k = \frac{x - x^{k+1-i}}{x^{k+i} - x^{k+1-i}}. \tag{19}$$

Notice that there are no restrictions on the smoothness of the basis functions between elements, which is helpful in cases of non-smooth solutions (Hesthaven and Warburton, 2008). To use higher order approximations we need to construct a higher order basis function space that requires more degrees of freedom per each element (details in Hesthaven and Warburton (2008)).

3.2 General scheme.

Let us consider the linear conservation law

$$\frac{\partial \mathbf{u}}{\partial t} + \frac{\partial \mathbf{f}}{\partial \mathbf{x}} = 0, \qquad \mathbf{x} \in \Omega, \tag{20}$$

which has $\mathbf{u}$ as the unknown function, $\mathbf{f}$ as the flux, and $\mathbf{x}$ and t as space and time independent variables respectively. Then, if the solution is considered as a linear approximation $u_h \in V_h$, the definition of the residual can be established as

$$x \in D^k : \qquad \Re_h(x,t) = \frac{\partial f_h^k}{\partial x} + \frac{\partial u_h^k}{\partial t}. \tag{21}$$

Following the Galerkin approach, the residual must fulfill the condition of orthogonality to the basis functions ℓ_i^k. If the inner product between two scalar functions, u and v, in our function space is defined as

$$(u,v)_{D^k} = \int_{D^k} uv dx, \tag{22}$$

the condition that will allow us to solve eqn. (20) is that the residual and the basis functions $\ell_i^k \in V_h$ are orthogonal to each other. Which means, that the inner product between the residual and every test function ℓ_i^k is equal to zero

$$\int_{D^k} \Re_h(x,t)\ell_i^k(x)dx = 0. \tag{23}$$

The local solution appears not to be unique at the interface if we recall that the elements share points at their boundaries. In order to work out this problem, the Gauss theorem can be applied to get

$$\int_{D^k} \frac{\partial u_h^k}{\partial t}\ell_i^k - \frac{\partial \ell_i^k}{\partial x} f_h^k = -[f_h^k \ell_i^k]_{x^k}^{x^{k+1}}, \tag{24}$$

where the term $-[f_h^k \ell_i^k]_{x^k}^{x^{k+1}}$ is understood as the link connecting elements. In more detail, the elements D^k and D^{k+1} depend on the flux at position x^{k+1}, which is the point that both share. Now, a numerical flux, f^*, can be introduced as the unique value to be used at the interface between elements and it is obtained by combining information from both. The numerical flux f^* can be inserted into equation (25)

$$\int_{D^k} \frac{\partial u_h^k}{\partial t}\ell_i^k - \frac{\partial \ell_i^k}{\partial x} f_h^k = -[f^* \ell_i^k]_{x^k}^{x^{k+1}}, \quad \text{weak form} \tag{25}$$

and, by applying the Gauss theorem again,

$$\int_{D^k} \Re_h(x,t)\ell_i^k(x)dx = [(f_h^k - f^*)\ell_i^k]_{x^k}^{x^{k+1}}, \quad \text{strong form.} \tag{26}$$

Equations (26) and (27) introduced the weak and strong forms of the DG-FEM scheme for a general scalar conservation law (equation (20)). It is of great importance to include our knowledge of the physical phenomena when computing it.

Finally, developing the weak and strong scheme, we get

$$M^k \frac{\partial u_h^k}{\partial t} - (S^k)^T f_h^k = f^*(x^k)l^k(x^k) - f^*(x^{k+1})l^k(x^{k+1}), \tag{27}$$

and

$$M^k \frac{\partial u_h^k}{\partial t} - (S^k) f_h^k = (f_h^k(x^{k+1}) - f^*(x^{k+1}))l^k(x^{k+1}) - (f_h^k(x^k) - f^*(x^k))l^k(x^k). \tag{28}$$

where the mass and stiffness matrices are given by

$$M_{ij}^k = \int_{D^k} l_i^k(x)l_j^k(x)dx, \qquad S_{ij}^k = \int_{D^k} l_i^k(x)\frac{dl_j^k(x)}{dx}dx \tag{29}$$

The DG-FEM has a local mass matrix M, which represents less computational costs for time dependent problems. Moreover, a careful design of the numerical flux f^* leads to stable schemes, by taking the underlaying physics of our PDE, in our case, the propagation of a discontinuity.

3.3 The Eikonal as a 1D Advection Equation.

Our second section introduced the form of the dynamic H-J equation (15), and the concepts mentioned so far in this section focused on solving equations of the form (20). Let us now merge both equations into a numerical scheme that can be solved by the DG-FEM. In this work the goal is the 1D eikonal equation, that simplifies the term $c(\mathbf{x})\nabla_{\mathbf{x}}\phi(\mathbf{x},t)$ form equation (15) to $c(x)(\partial\phi(x,t)/\partial x)$. Notice that the values of ϕ now vary only with respect to the x direction and the time t. In order to respect our notation, consider $\phi(x,t) = u(x,t)$ and the 1D dynamic H-J equation is then

$$\frac{\partial u(x,t)}{\partial t} \pm c(x)\left|\frac{\partial u(x,t)}{\partial x}\right| = 0, \tag{30}$$

where the sign $\pm$ describes if the propagation is to $+x$ or to $-x$. This $\pm$ term is the responsible of the direction of the flow of information. We recognize that at the source there is a singularity where the direction of propagation is not defined. If we set our initial condition at a $+\xi$ distance away from the source, and we define a propagation to the right, we end up with the advection PDE (31). If the spatial derivative of $u(x,t)$ is positive: we must insure this feature while solving

the PDE in time. We choose an initial condition $u(x,0)$ with this property and, then, we chech that this property is fulfilled during the time integration at a given numerical error. Our approach will be, from now, on a $+x$ direction of flow, with an initial condition where the wavefront is far from the singularity of the source at infitesimal distance ξ. Our PDE now is

$$\frac{\partial u(x,t)}{\partial t} + c(x)\frac{\partial u(x,t)}{\partial x} = 0, \tag{31}$$

subjected to the initial and boundary conditions

$$u(x,0) = \begin{cases} 1 & if x < \xi, \\ 0 & if x \geq \xi. \end{cases}$$

and the boundary conditions

$$u(x_b,t) = \begin{cases} 1 & if x_b = x_l, \\ 0 & if x_b = x_r. \end{cases}$$

where x_l and x_r correspond to the fisrt and last node coordinate of our 1D physical domain, and the value 1 is a normalized quantity.

Taking the PDE (31) the p-th order approximated local solution of our numerical scheme can be obtained as

$$u_h^k(x,t) = \sum_{i=0}^{N_p} u_h^k(x_i^k,t)\ell_i^k(x), \tag{32}$$

where $N_p = n+1$ is the number of nodes inside one element, k represents the local element and ℓ_i^k are the Linear Lagrangian polynomials (19). Using (28), we reformulate our equation (31) as follows

$$M^k\frac{du_h^k(x,t)}{dt} + c(x)S^k u_h^k = [\ell^k(x)(c(x)u_h^k - (c(x)u)^*)]_{x_l^k}^{x_r^k}, \tag{33}$$

or multiplying by $(M^k)^{-1}$

$$\frac{du_h^k(x,t)}{dt} = -c(x)(M^k)^{-1}S^k u_h^k(M^k)^{-1}[\ell^k(x)(c(x)u_h^k - (c(x)u)^*)]_{x_l^k}^{x_r^k}. \tag{34}$$

Equation (34) shows the scheme to be used in this work to approximate the values of $\mathbf{u}_t$.

Gottlieb and Shu (1998) showed that spurious oscilations could be generated by a non Time Variation Diminishing (TVD) linear stable Runge-Kutta. Therefore, we follow the scheme of Cheng and Shu (2007), where a third-order TVD Runge Kutta is implemented to perform the time integration of (34). First we simplify equation (34) as

$$\frac{du_h^k(x,t)}{dt} = L(\mathbf{u}), \tag{35}$$

where $L(\mathbf{u})$ is the right hand side of equation (34). Then, the time integration from the time step n to $n+1$ implies the following computations

$$\mathbf{u}^{(1)} = \mathbf{u}^n + \Delta t L(\mathbf{u}^n), \tag{36}$$

$$\mathbf{u}^{(2)} = \frac{3}{4}\mathbf{u}^n + \frac{1}{4}\mathbf{u}^{(1)} + \frac{1}{4}\Delta t L(\mathbf{u}^{(1)}), \tag{37}$$

$$\mathbf{u}^{n+1} = \frac{1}{3}\mathbf{u}^n + \frac{2}{3}\mathbf{u}^{(2)} + \frac{2}{3}\Delta t L(\mathbf{u}^{(2)}), \tag{38}$$

where Δt is the time step integration. In order to obtain a stable discrete solution, Δt must be chosen respecting

$$\Delta t \leq \frac{CFL}{\max c(x^k)} \min_{k,i} \Delta x_i^k. \tag{39}$$

where CFL is a Courant-Friedrichs-Levy-like constant, the terms $\Delta x_k = x_{k_i} - x_{k_{i+1}}$ and $\max c(x^k)$ is the minimum local grid size and maximum local wave speed respectively.

3.4 Numerical flux: Central or Upwind?

The choice of the numerical flux is a crucial decision that impacts directly the stability of the scheme (34). The form of $u^* = u^*(u_h^-, u_h^+)$, depends on the information coming from out (u_h^+), and inside (u_h^-) the local element. A further lecture on fluxes can be found in Hesthaven and Warburton (2008). We explore the Lax-Friederichs flux in our scheme along $\hat{\mathbf{n}}$, wich corresponds to the orthogonal direction to the element face, so that

$$f^{LF}(u^-, u^+) = \frac{u(^-) + u(^+)}{2} + \frac{C}{2}\hat{\mathbf{n}} \cdot (u^- - u^+), \tag{40}$$

where the constant C determines if the numerical flux is upwind ($C = 0$), or central ($C = 1$). The central flux takes into account the information of the two elements sharing the interface, while the upwind also considers the defined direction of propagation. In figure 10 we ilustrate how the different numerical fluxes can affect the solution of the propagation of a Heaviside function as the following initial condition (non-smooth solution) is set

$$u(x,0) = \begin{cases} 1 & if x < 0.5, \\ 0 & if x \geq 0.5. \end{cases} \tag{41}$$

and the boundary conditions

$$u(x_b,t) = \begin{cases} 1 & if x_b = 0, \\ 0 & if x_b = 40. \end{cases} \tag{42}$$

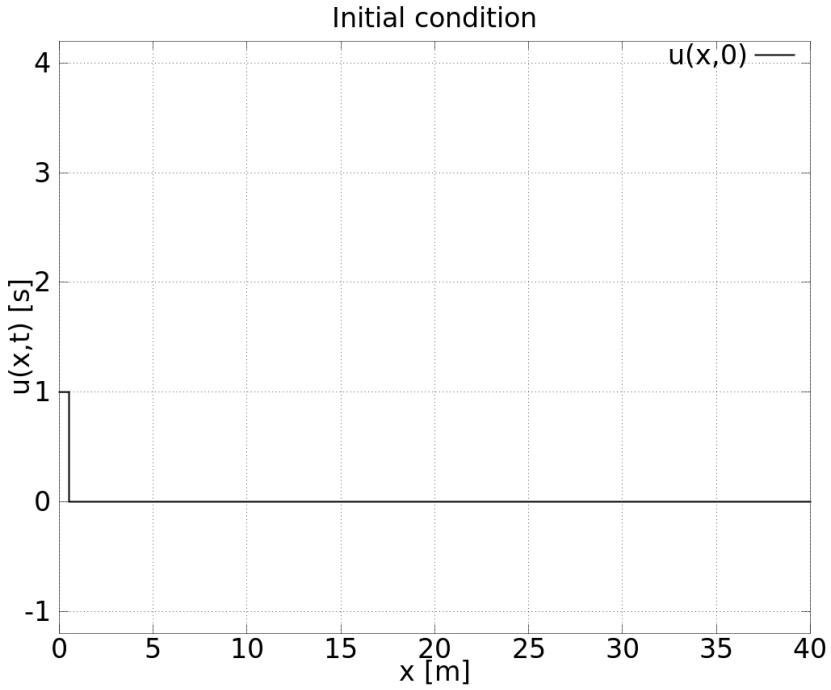

Figure 10: Initial condition, Heaviside (41). The wavefront is represented as a discontinuity at $\xi = 0.5$. This is the initial condition for the results presented in figure 12.

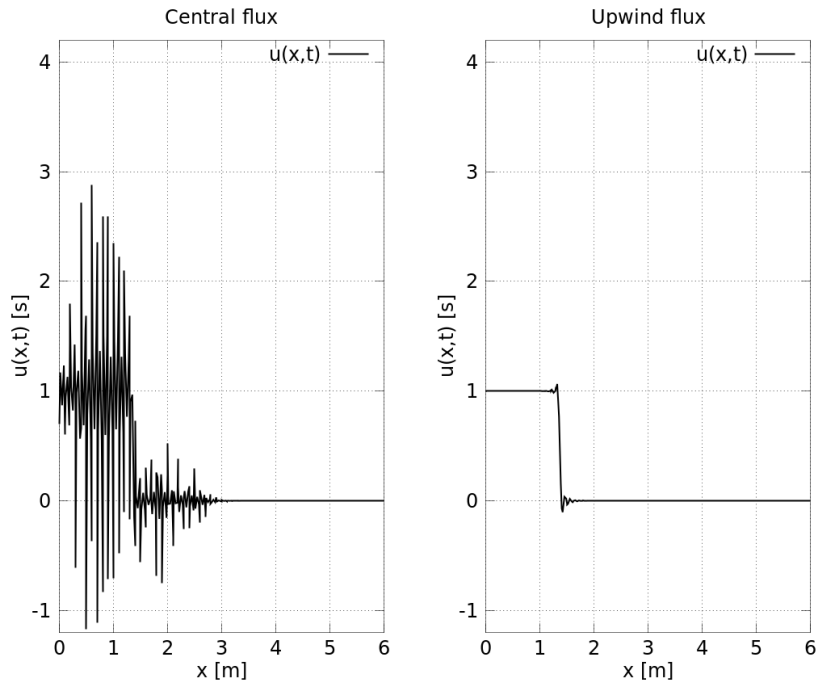

Figure 11: Comparison between solutions to (31), after 1000 integration time steps, obtained by applying central and upwind fluxes. The initial condition is the Heaviside function (41) in figure 11. The solution by applying a central flux (left) is non-stable and presents more spurious oscilations near to the propagating discontinuity in comparison with the upwind solution (right).

The comparison between the results obtained by central and upwind fluxes clearly shows that the upwind flux is the optimal among both. This is because the upwind flux always takes information from where it is coming. This allows to better track the discontinuity. Unfortunately, upwind fluxes introduce some artificial diffusion that reduces the total energy of the system.

3.5 Travel times by tracking the wavefront, initial and boundary conditions.

Taking into account our observations in figure 11, we decide to apply our proposed scheme using an upwind flux in the defined direction of propagation $(+x)$. Nevertheless, we still recognize the presence of spurious oscilations. It is clear that the oscilations are associated with the propagation of a discontinuity (non-smooth solutions). However, we are mainly interested in propagating wavefronts which can be seen as discontinuities. Therefore, we stablish as an initial condition a function with a well-known shape that can be tracked during the propagation.

The simplest function to track is a linear trend. Then, our strategy is to define a function with a discontinuity, which corresponds to our wavefront, and a linear trend in front of it (see figure 12). During the propagation the linear trend will also propagate at the same speed of the discontinuity, and knowing the exact form of the linear trend we will allow us to detect where the wavefront is. The initial condition is as follows

$$u(x,0) = \begin{cases} 1 & if x < \xi, \\ \frac{x-\xi}{10} & if x \geq \xi. \end{cases} \tag{43}$$

and boundary conditions

$$u(x_1,t) = \begin{cases} 1 & if x_b = x_l, \\ \frac{x_r - x(wavefront)}{10} & if x_b = x_r. \end{cases} \tag{44}$$

In order to use the linear trend to detect the location of the wavefront a linear regression must be performed. In homogeneous media, the linear trend propagates at the same wave speed as the wavefront, which preserves the original form of the function and the linear regression can be done at any element, where the trend is present, to locate the wavefront position. On the contrary, in heterogeneous media the information conforming the trend tavels at different speeds, this speeds deform the function and the linear regression must be performed at the nearest element to the discontinuity. A criteria is applied to detect the nearest element to the wavefront, where the solution $\mathbf{u}_h$ and its spatial derivative is stable. Then, a subset of $\mathbf{u}_h$ is taken from the stable linear trend and a linear regression is used to track the position of the wavefront at each time step of the integration (figure 12).

In addition, the oscilations associated with the evolving wavefront are also propagating. As the wavefront moves, the oscilations propagate further. In order to decrease the effect of the oscilations a re-setting of the initial condition at each n integration time steps is applied. Once the wavefront is located by the linear regression, we re-set the initial condition at the

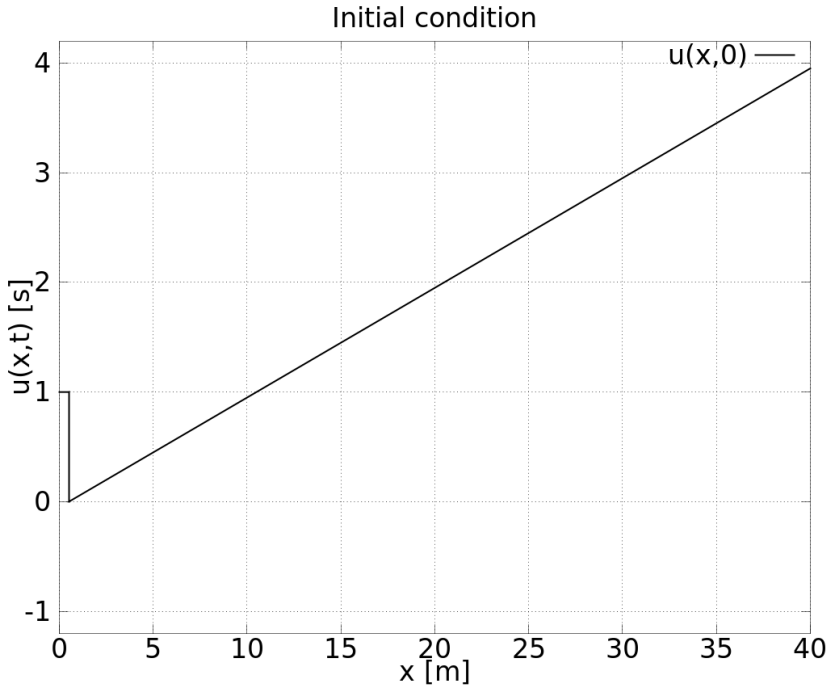

Figure 12: Initial condition (42). The wavefront is represented as a discontinuity at $x = 0.5$ followed by a linear trend. The domain is discretized by 400 elements of $x = 0.1$ length, from $x = 0$ to $x = 40$. This is the initial condition for the results presented in figure 13.

wavefront position $x(wavefront)$, which means to set $\mathbf{u}_h = 1$ at positions behind the wavefront location, and $\mathbf{u}_h = \frac{x - x(wavefront)}{10}$ for $x \geq x(wavefront)$. Moreover, a weaker criteria to locate the nearest stable element is applied to be nearer from the wavefront once the oscilations are removed (figure 14).

Summarizing, the numerical scheme (34) is used by applying an upwind flux (39) in the $+x$ direction with a local wave speed $c(x)$. The time integration of (34) is done through a third order TVD Runge Kutta (35 - 38). Our initial and boundary conditions (43 - 44) allow us to track the wavefront position at any time step by implementing our linear regresion. And the propagating oscilations effect is vanished by our re-set of the initial condition at the wavefront position. In the next section we test our numerical scheme with three cases, where we estimate the travel time functions of 1D wave propagation along different media.

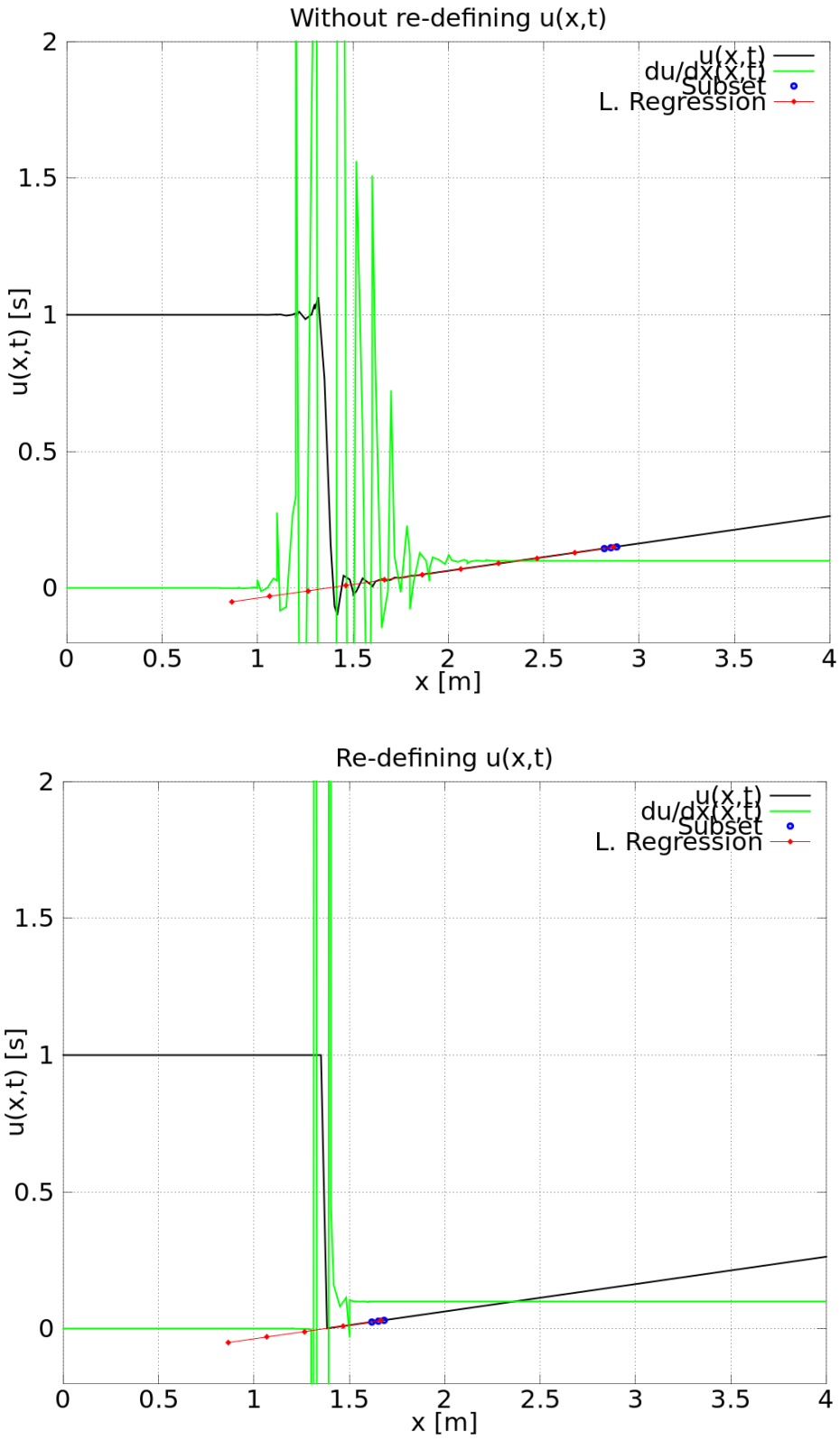

Figure 13: Approximated solutions after 1000 time steps. The physical domain is discretized by 400 elements of $x = 0.1$ [m], p_4 interpolation polynomials, $CFL = 0.1$. The wave speed is homogeneous, $c(x) = 0.4$ [m/s]. This figure ilustrates how the re-definition of $u(x,t)$ at each time integration step reduces the propagation of oscilations (down) compare to the solution that is not re-defined (up). The nearest stable element used for the linear regression is closer to the discontinuity when the solution is re-defining.

4 Applied numerical examples

For the next numerical examples the initial and boundary conditions are given by

$$u(x,0) = \begin{cases} 1 & if x < 0.5, \\ \frac{x-0.5}{10} & if x \geq 0.5, \end{cases} \tag{45}$$

$$u(x_1,t) = \begin{cases} 1 & if x_{initial} = 0, \\ \frac{40-x(wavefront)}{10} & if x_{final} = 40, \end{cases} \tag{46}$$

which are a specific case of the conditions (43) and (44) that we decide arbitrarily.

For all the three examples, the values of $u_h(x,t)$ are re-defined at every time integration step to reduce the effect of the propagating oscilations. The values are re-set, given $\mathbf{u}_h = 1$ at positions behind the wavefront location, and $u_h = \frac{x-x(wavefront)}{10}$ for $x \geq x(wavefront)$. We use a CFL constant very small to avoid unstable solutions,$CFL = 0.1$.

4.1 Example 1: Homogeneuous speed medium.

Our first example is the wavefront propagation along a 1D homogeneous medium of wave speed $c(x) = 0.4$ [m/s]. The boundaries of our physical domain are at $x_l = 0$ [m] and $x_r = 40$ [m]. The final time of computations is set to $t_{final} = 50$ [s]. The wavefront is located at each time step and the travel time is plotted (figure 14). A summary of the parameters used to compute the results in figure 14 are provided in table 2.

Table 2: Summary of the parameters related to the numerical example in the homogeneous medium. The symbols correspond to: h element size, p order of polynomials used, t_{final} final time computed, $c(x_{initial})$, $c(x_{final})$ initial and final wave speed, $t_{samples}$ time integretion steps, N_{L1}, N_{L2} global errors using Norm L1 and L2, $N_{elements}$ number of elements along the grid and N_{norm} samples used to estimate de misfits.

Parameter	Value	Parameter	Valuer
h	0.025 [m]	$t_{samples}$	92661 time samples
p	4th order	N_{L2}	5.4229e-03 [s]
t_{final}	50 [s]	$N_{elements}$	1600
$c(x_{initial})$	0.4 [m/s]	N_{norm}	100 points used
$c(x_{final})$	0.4 [m/s]		

In order to understand the impact of the element size on the estimated solution, more simulations with different element size were performed. For the same example in the homogenous media, the different structured grids had element sizes of $h = [0.25, 0.1, 0.05, 0.025, 0.0125]$ [m]. A norm L2 is used to estimated the misfits between our estimated travel time and the analytical values, the results are plotted in figure 15.

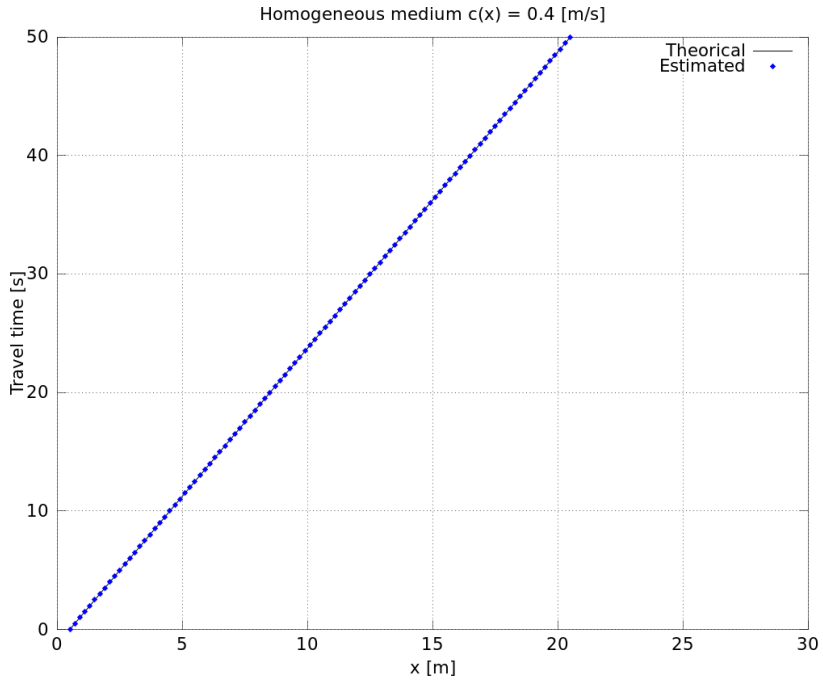

Figure 14: Travel time plot of the wavefront propagation along an homogenous 1D medium. The wave speed is $c(x) = 0.4$ [m/s]. 100 samples conformed our estimated travel time (blue dotted line), a sample is taken each 926 time steps. The theoretical values of travel time (black solid line) are computed by a discrete summation along the domain for each estimated position. Notice that in the homogenous medium, the travel time values draw a straight line which slope value is the inverse of the wave speed. See table 2 for more information.

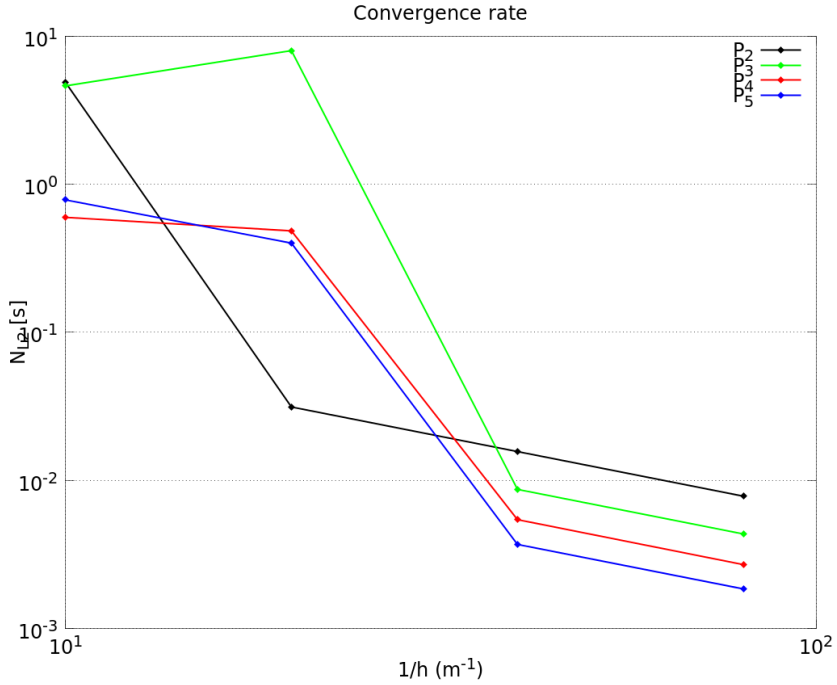

-5pt

Figure 15: Loglog plot of the Norm L2 applied to the misfits between analytical values of travel time and the values estimated on structured grids with different element sizes. The size of the element are $h = [0.1, 0.05, 0.025, 0.0125]$ [m] (dots). Each line corresponds to the order of the polynomials used, as shown in the legend. The medium is homogeneous with a wave speed $c(x) = 0.4$ [m/s].

4.2 Example 2: Heterogeneuous increasing speed medium.

Now, we track our wavefront along a medium which wave speed increases monotonically constant. The initial wave speed is $c(x_{initial}) = 0.40$ [m/s] at $x = 0$ [m], the increment of speed is $dc = 0.01$ [m/s] each 0.1 [m], giving as a result a last wave speed of $c(x_{final}) = 4.40$ [m/s] at $x = 40$ [m]. A table of summary of the parameters used to compute the results shown in figure 16 are provided in table 3.

Table 3: Summary of the parameters related to the numerical example 2. The symbols used here are the same as for table 2 and 3.

Parameter	Value	Parameter	Valuer
h	0.025 [m]	$t_{samples}$	406781 time samples
p	4th order	N_{L2}	0.61065 [s]
t_{final}	20 [s]	$N_{elements}$	1600
$c(x_{initial})$	0.4 [m/s]	N_{norm}	100 points used
$c(x_{final})$	4.4 [m/s]		

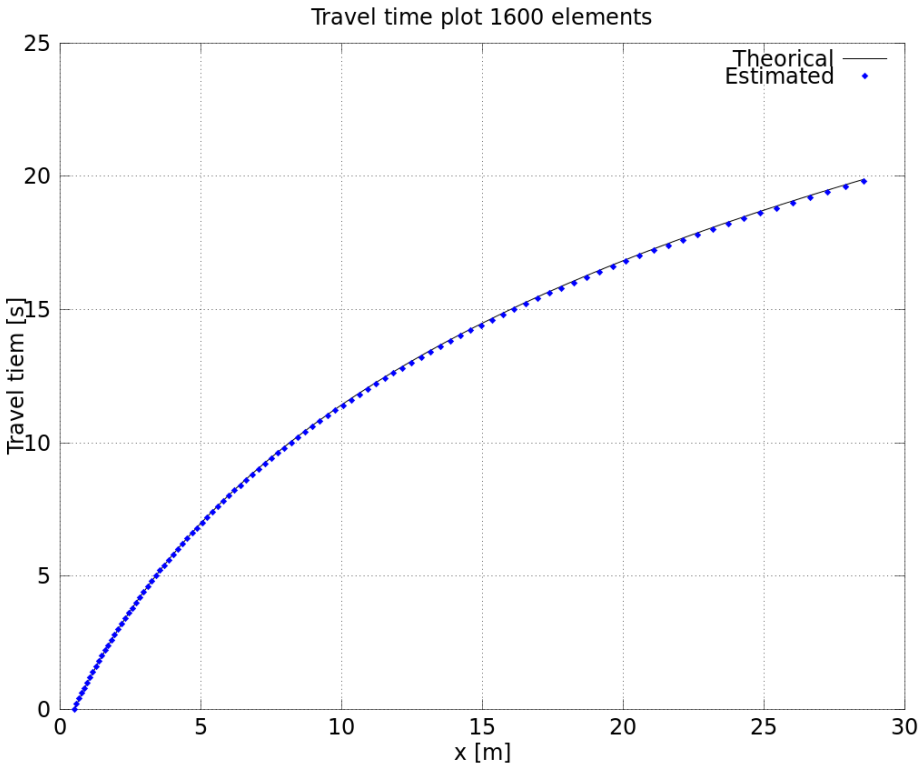

Figure 16: Travel time plot of the wavefront propagation in a medium with a monotonical increment of wave speed. The initial wave speed is $c(0) = 0.4$ [m/s], the increment is $dc = 0.01$ [m/s] each $dx = 0.1$ [m]. The element size is $h = 0.025$ [m], and the order of polynomials is 4th. The final time is $t = 20$ [s]. 100 samples conformed our estimated travel time (blue dotted line), a sample is taken each 4067 time steps. The theoretical values of travel time (black solid line) are computed by a discrete summation along the domain for each estimated position. Notice that the largest misfits are at the furthest distance from the source.

Different structured grids are again used to verify that our approximation convergence the solution by decreasing the element size. The simulations are done for values of $h = [0.1, 0.05, 0.025, 0.0125]$ [m]. Figure 17 shows the decrement of the misfit for shorter elements.

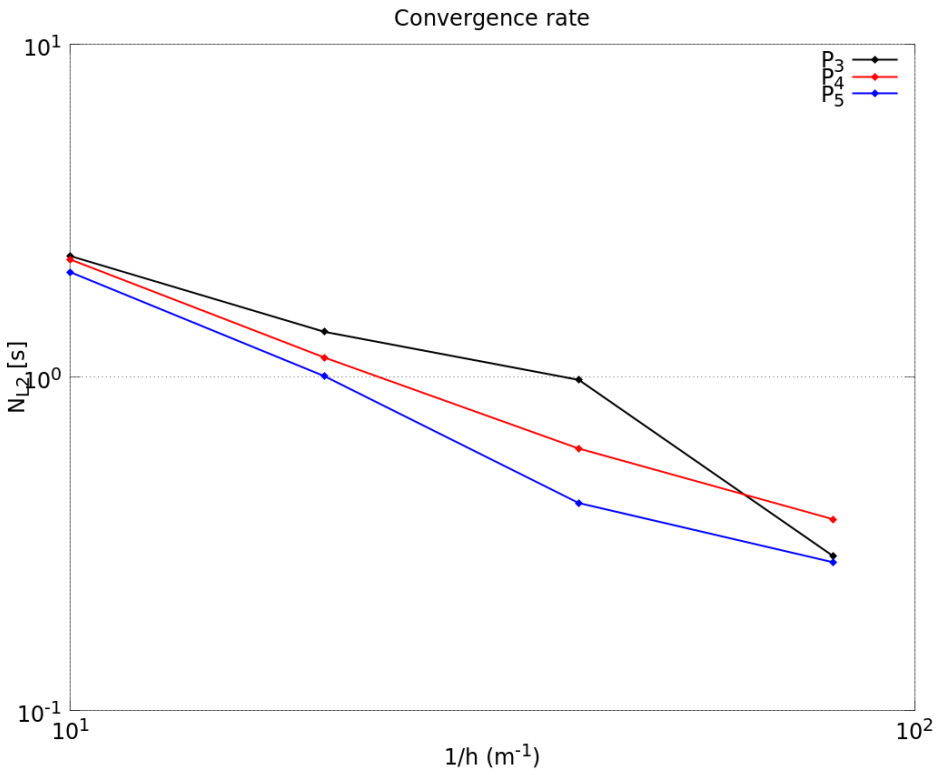

Figure 17: Loglog plot of the Norm L2 applied to the misfits between theoretical values of travel time and the values estimated for different grids. The size of the element are $h = [0.1, 0.05, 0.025, 0.0125]$ [m] (dots). Each line corresponds to the order of the polynomials used, as shown in the legend. Thhis global errors are related to the propagation along a heterogeneous medium with a monotonical increasing of wave speed.

4.3 Example 3: Medium with a Low-velocity zone.

This last example implies an increment an decrement of the wave speed along our discrete medium. The boundaries still the same, $x_l = 0$ [m] and $x_r = 40$ [m]. The wave speed increseas at each $dx = 0.1$ [m] from $c(0) = 0.4$ [m/s] to $c(5) = 0.9$ [m/s] with a $dc = 0.01$ [m/s]. Then, the wave speed decreases with the same rate until $c(10) = 0.4$ [m/s]. The speed remains constant (0.4 [m/s]) until $x = 15$ [m], where a monotonic increment starts with $dc = 0.01$ [m/s]. The last value of wave speed is $c(40) = 2.9$ [m/s].

Using the conditions (45) and (46), we track our wavefront along this medium with a low-wave speed zone. The final time of computation is 40 [s]. As for the first and second examples, table 4 lists the parameters involved in the results shown in figure 28.

Figure 19 shows how the accuracy of the appromation increases by considering shorter element size. We compute the global erros using the norm L2 for grids with different size element. The values consider are as in example one and two, $h = [0.1, 0.05, 0.025, 0.0125]m/$.

Table 4: Summary of the parameters related to the numerical example 3. The symbols used here are the same as for table 2 and 3.

Parameter	Value	Parameter	Valuer
h	0.025 [m]	$t_{samples}$	535670 time samples
p	4th order	N_{L2}	0.37346 [s]
t_{final}	40 [s]	$N_{elements}$	1600
$c(x_{initial})$	0.4 [m/s]	N_{norm}	100 points used
$c(x_{final})$	2.9005 [m/s]		

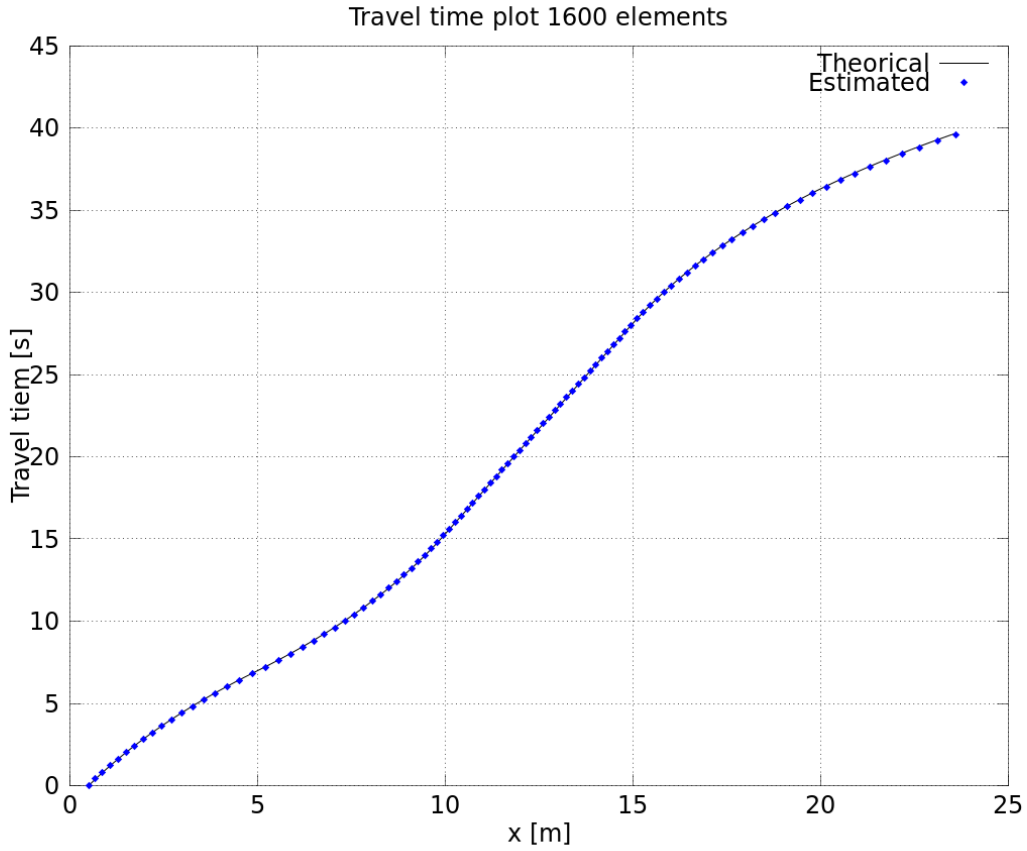

Figure 18: Travel time plot of the wavefront propagation in a medium with a low-wave speed zone. The initial wave speed is $c(0) = 0.4$ [m/s], the increment is $dc = 0.01$ [m/s] until $x = 5$ [m], at this coordinate the speed decreases $dc = -0.01$ [m/s] each 0.1 [m]. The decrement stops at 10 [m] where the speed is constant $c = 0.4$ [m/s]. A last increment of the speed starts at 15 [m], with a $dc = 0.01$ [m/s]. 100 samples conformed our estimated travel time (blue dotted line), a sample is taken each 5356 time steps. The theoretical values of travel time (black solid line) are computed by a discrete summation of the theoretical travel times for each estimated position. Notice that the misfits are are positives when the speed increases, on the contrary the misfits are negative when the speed decreases.

Finally, an analysis hp is provided for this third numerical example. The order of polynomials used go from 2nd to 5th order. As for the convergence test (figures 15, 17 and 19), we use the grids with $h = [0.1, 0.05, 0.025, 0.0125]$ [m]. Figure 20 shows this comparison between the global errors achieved (Norm L2) and computation time in [s].

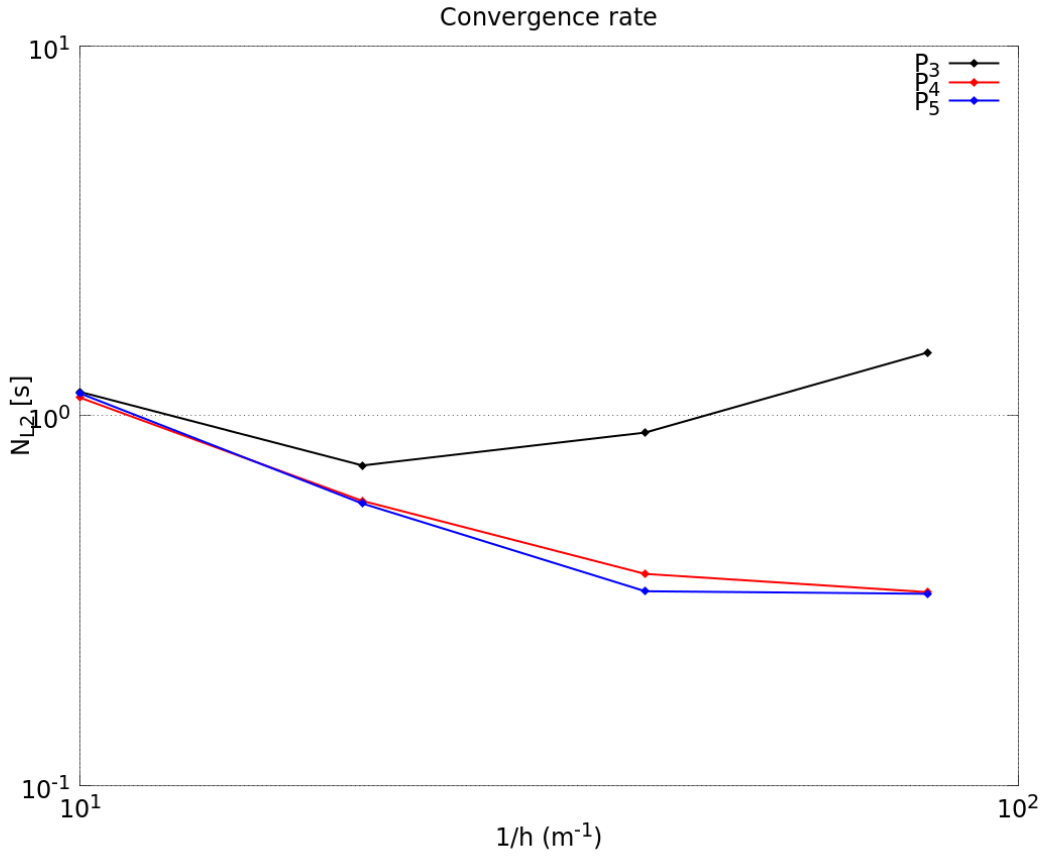

Figure 19: Loglog plot of the Norm L2 applied to the misfits between theoretical values of travel time and the values estimated. The sizes of the elements used are $h = [0.1, 0.05, 0.025, 0.0125]$ [m] (dots). Each line corresponds to the order of the polynomials used, as shown in the legend. The medium is heterogeneous with a low-wave speed zone (figure 20).

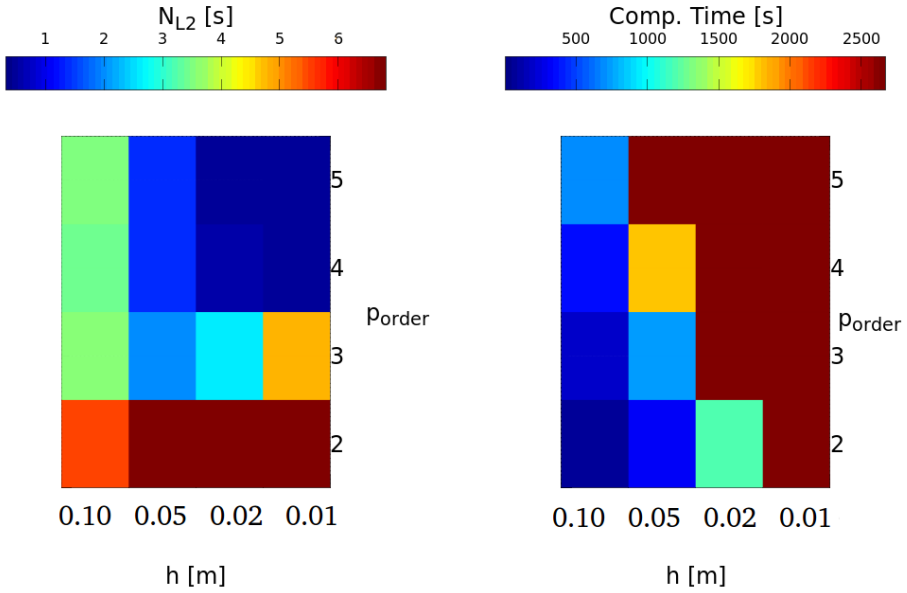

Figure 20: Analysis P-H of the results obtained from the third numerical example. Polynomials of order 2, 3, 4, 5 as well as the size of the elements $h = [0.1, 0.5, 0.025, 0.0125]$ [m] are used in this plot. Estimation with higher order polynomials show to be more accurate but dramitiaclly expensive in terms of computation time. Polynomials of third order with grids of $h = 0.025$ [m] balance correctly the computation time with the L2 norm.

5 Conclusions: discussion and perspectives

We successfuly use the DG-FEM to solve the 1D eikonal equation as a 1D advection equation with a defined upwind direction of flow. However, there were several difficulties related to the instabilities near to the discontinuity. Even though our scheme managed to avoid this problems by redefining the solution at each time step, a more desirable approach must be implemented as the one shown by Cheng and Shu (2007), Bokanowski et al. (2011) and Bokanowski et al. (2014). As the re-definition of the solution at each time step necessarily implies to locate the wavefront at a node, it is definetely a source of errors impacting the travel time estimation.

The direction of the information's flow was prescribed by us from the beggining of the formulation of the problem. In order to completely solve the eikonal equation, we must not rely on our decision. The decision must be taken independently of the user, and it shall consider a propagation from a high-information location to a low one. To do so, criteria of minimum entropy might be applied into the numerical scheme, as described by Cheng and Shu (2007) and Bokanowski et al. (2011, 2014). These criteria might decrease the oscilations associated with the discontinuity, and as a consequence, the direction of flow could be distinguished.

The results shown in figure 15, 17 and 19, suggest that our aproximated travel time values converge to an acceptable level of accuracy just by refining our grid. Nevertheless, we consider that our value of CFL ($CFL = 0.1$) penalized our computations, and further numerical exercises with larger values of CFL might be interesting. Figure 20 also shows that higher order approximations are more accurate. Nonetheless, the computational costs increase dramatically if we consider polynomials higher than 4th order.

This scheme can be extended to 2D and 3D. Cheng and Shu (2007), Bokanowski et al. (2011, 2014) have already shown that it is possible and accurate enough. However, we must first apply an entropic criterion to remove our instabilities. Once this is done, a new numerical flux needs to be built in a way that it implies an independent decision of the direction of propagation. Finally, a $hp-$ adaptivity (Etienne et al., 2010) must be also included for 2D and 3D applications, as it is an efficient way to keep accuracy and low computational costs.

References

Bokanowski, D., Cheng, Y., and Shu, C.-W. (2011). A discontinuous galerkin solver for front propagation. *SIAM J. Scient. Comput.*, 33(2):923–938.

Bokanowski, O., Cheng, Y., and Shu, C.-W. (2014). A discontinuous galerkin scheme for front propagation with obstacles. *Numerische Mathematik*, v126:1–31.

Chapman, C. H. (2004). *Fundamentals of Seismic Wave Propagation*. Cambridge University Press, Cambridge.

Cheng, Y. and Shu, C.-W. (2007). A discontinuous galerkin finite element method for directly solving the hamilton–jacobi equations. *Journal of Computational Physics*, 223:398–415.

Crandall, M. C. and Lions, P. L. (1983). Viscosity solutions of hamilton-jacobi equations. *Transactions of the American Mathematical Society*, 277(1):1–42.

Crandall, M. C. and Lions, P. L. (1984). Two approximations of solutions of hamilton-jacobi equations. *Mathematics of computation*, 43(167):1–19.

Engquist, B., Runborg, O., and Tornberg, A. K. (2002). High-frequency wave propagation by the segment projection method. *Journal of Computational Physics*, 37:331–339.

Etienne, V., Chaljub, E., Virieux, J., and Glinsky, N. (2010). An hp-adaptive discontinuous galerkin finite-element method for 3-d elastic wave modelling,. *Geophys. J. Int.*, 183(2):941–962.

Gottlieb, S. and Shu, C.-W. (1998). Total variation diminishing runge-kutta schemes. *Maths. of Comput.*, 67-221:73–85.

Hauser, J., Sambridge, M., and Rawlinson, N. (2006). Phase space methods for multi-arrival wavefronts. *Exploration Geophysics*, 37:331–339.

Hesthaven, J. and Warburton, S. T. (2008). *Nodal Discontinuous Galerkin Methods Algorithms, Analysis and Applications*. Springer Science+Business Media, ISBN: 978-0-387-72065-4 DOI: 10.1007/978-0-387-72067-8.

Hu, C. and Shu, C.-W. (2004). A discontinuous galerkin finite element method for hamilton-jacobi equations. *SIAM J. Sci. Comput.*, 21-2:666–690.

Osher, S. and Fedkiw, R. (2003). *Level Set Methods and Dynamic Implicit Surfaces*. Springer-Verlag New York, Inc., ISBN 0-387-95482-1.

Osher, S., Kang, M., Shim, H., Tsai, Y.-H., and Cheng, L.-T. (2002). Geometric optics in a phase-space-based level set and eulerian framework. *Journal of Computational Physics*, 179:622–648.

Quian, J., Cheng, L.-T., and Osher, S. J. (2003). A level set based eulerian approach for anisotropic wave propagations. *Wave motion*, 37:365–379.

Rawlinson, N., Hauser, J., and Sambridge, M. (2007). Seismic ray tracing and wavefront tracking in laterally heterogeneous media. *Advances in Geophysics*, 49:203–267.

Sethian, J. (1999). *Level set methods and fast marching methods*. Cambridge University Press, Cambridge.

Thorton, S. T. and Marion, J. B. (1994). *Classical Dynamics of Particles and Systems*. Thomson Books/Cole, United States of America.

Vidale, D. (1988). Finite-difference calculation of travel time. *Bulletin of the Seismological Society of America*, 78:2062–2076.

Vidale, D. (1990). Finite-difference calculation of travel times in three dimensions. *Geophysics*, 55:521–526.

Vinje, V., Iversen, E., and Gjoystdal, H. (1993). Traveltime and amplitude estimation using wavefront construction. *Geophysics*, pages 1157–1166.

Virieux, J. and Farra, V. (1991). Ray tracing in 3-d complex isotropic media: an analysis of the problem. *Geophysics*, 56:2057–2069.

Virieux, J. and Lambare, G. (2014). Theory and observations - body waves: Ray methods and finite frequency effects. *empty*, 8:1–93.

Zhao, H. (2005). A fast sweeping method for eikonal equations. *Mathematics of computation*, 74:603–627.